Communications Physics

https://doi.org/10.1038/s42005-026-02795-1

Article in Press

Linking particle stress distributions in clogged silos and the avalanche size

Received: 1 December 2025

Accepted: 22 July 2026

Published online: 30 July 2026

Cite this article as: Zhou, G.G., Li, N., Cui, K.F. *et al.* Linking particle stress distributions in clogged silos and the avalanche size. *Commun Phys* (2026). https://doi.org/10.1038/s42005-026-02795-1

Gordon G. D. Zhou, Nanjun Li, Kahlil Fredrick Ermac Cui, Jidong Zhao, Lu Jing, Xueqiang Lu & Yunxu Xie

Linking particle stress distributions in clogged silos and the avalanche size

Gordon G. D. Zhou[1,2,3], Nanjun Li[1,2,*], Kahlil F. E. Cui[1,2], Jidong Zhao[1,4], Lu Jing[5], Xueqiang Lu[1,2] & Yunxu Xie[1,2]

[1]Key Laboratory of Mountain Hazards and Engineering Resiliences / Institute of Mountain Hazards and Environment, Chinese Academy of Sciences, Chengdu 610000, China.

[2]University of Chinese Academy of Sciences, Beijing 100000, China.

[3]Sino-Italian Joint Laboratory on Geological and Hydrological Hazards, Chengdu 610000, China.

[4]The Hong Kong University of Science and Technology, Hong Kong 999077, China.

[5]Institute for Ocean Engineering, Shenzhen International Graduate School, Tsinghua University, Shenzhen 518055, China.

*Corresponding author: lnj@imde.ac.cn

ABSTRACT. Discrete bodies passing through narrow openings in silos can become clogged, forming a quasi-static assembly whose stress state reflects the preceding discharge process. Although central to clog stability and unclogging, this stress state does not fully follow either Janssen-type or hydrostatic models, suggesting history-dependent mechanics. Here we show that stress decreases with opening size through the number of particles released before clogging, defined as the avalanche size. Scaling analysis identifies two transitions, with stress resembling that of sealed bodies below a minimum avalanche size but approaches a minimum asymptotic value as avalanche size increases. This decrease is accompanied by reduced effective particle weight and increased sidewall shear support. Boundary force chains orient toward silo walls, while central clogging arches increase the normal-to-parallel stress ratio along force-chain directions, leading local stress to decrease with depth. This study provides insights into the mechanisms underlying stress variations in particle assemblies clogged above openings.

Key words: clogged state, stress distribution, avalanche size

Introduction

Unlike fluids, systems composed of discrete particles exhibit inherently complex flow behavior when particles are strongly confined and boundary effects dominate[1,2]. It is commonly observed that particles exiting through apertures can stabilize each other at the opening by forming arch-like structures[3–6]. These arches redistribute the load of the outflowing granular mass, ultimately clogging the flow while sustaining their own structural integrity. An analogous system is crowd evacuation through narrow doors, a discrete two-dimensional system with an opening, where individuals possess self-driven velocities arising from local rearrangements and interactions, resulting in intermittent flow and blockages at the constriction. Determining the forces between individuals becomes critical because clogging can lead to severe injuries[7,8]. In three-dimensional silo systems used in food processing, mining, and materials handling, small silo openings are commonly used to regulate gravity-driven flow, preventing overload of downstream systems and maintaining a stable material supply, yet this practice inevitably promotes clogging, making reliable discharge difficult to sustain[9–14]. A common strategy to reduce clogging at narrow openings is to apply vibration, which destabilizes the frictional forces holding the clogged particles together[4,9,15]. Therefore, it is necessary to understand the stress distribution in a clogged state in order to provide the sufficient energy required to de-clog[16,17]. These systems can be idealized as containers with open orifices, commonly modeled as silos. This simplified yet widely adopted geometry enables controlled exploration of clogging behavior and the resulting stress distributions. The investigation of stress distribution in narrow-opening systems provides valuable guidance for crowd safety and a better understanding of the unclogging process[5,8,17,18].

The pressure distribution of fluid hydrostatics within a container is well-established and widely understood, however, the static pressure distribution of granular media remains largely unexplored. The fundamental challenge arises from the fact that granular materials possess a discrete and frictional nature, leading to stress distributions that deviate from traditional fluid-like behavior. The stress distributions are primarily dictated by factors such as preparation history and the structure of the silo[19]. In an idealized system where granular materials are stored in a boundary-free or near-frictionless container, the pressure at a given depth is expected to follow a simple hydrostatic relation, increasing proportionally with depth in accordance with the so-called liquid stress distribution[20]. In the absence of lateral frictional forces, the entire weight of the granular column is supported by the particles beneath it, analogous to a liquid in a container.

The presence of boundary wall friction provides support to granular media, leading to an initial increase in pressure with depth that eventually saturates at a finite value—a phenomenon known as the Janssen effect. This effect arises because the friction between the particles and the container walls allows for the transfer of vertical into horizontal stress, resulting in the sidewalls providing upward frictional support to the granular material. Consequently, the pressure does not continuously increase with depth but instead reaches a saturation point. Recent studies have further revealed that under specific conditions, such as in narrow containers, sidewall friction can instead enhance particle compression, leading to confined pressures that exceed the predictions of the liquid stress distribution. This counterintuitive behavior is referred to as the reverse Janssen effect[21]. These stress distributions are generally uniform across the radial direction of the container.

When particles are flowing through the bottom opening of a silo, internal pressures are low and are minimum near the orifice wherein greater discharge results in lower flowing pressures[22,23]. Although pressures once again increase when the flow is jammed, it does not homogenize throughout the container, as in completely sealed systems where there is no flow[24]. Instead, pressures remain relatively low in the vicinity of the orifice where its magnitude depends on the opening size[5]. Despite this understanding, the mechanisms that lead to low (high) static pressures when the silo opening is large (small) remain poorly understood.

The silo opening determines the average number of released particles prior to clogging, referred to as the avalanche size[25–27]. The avalanche size is governed by stochastic processes near the orifice, where random particle collisions may lead to the formation of blocking arches[3,26–28]. As particles are released from the opening, a cavity forms above, and other particles in the silo move toward the opening to fill the cavity[22,23]. The displacement of internal particles varies with their location. For example, particles near the outer boundaries may remain stationary due to repose angle, forming a dead zone, while particles in the center of the silo collapse toward the centerline, forming an arch structure[23,29,30]. The force chains near the silo depend on the particle re-arrangement following an avalanche, suggesting that the Janssen or the liquid stress equations may no longer be applicable when an opening is present. Moreover, the direct relationship between avalanche size and stress distribution remains undetermined. Defining this relationship is crucial for modeling stress distribution in clogged silos.

Here we use discrete element method (DEM) simulations to investigate how stress distributions in silos with different outlet sizes compare with predictions from classical models, including the Janssen and liquid stress formulations. We find that the stress distribution is systematically linked to the avalanche size, and this relationship can be quantitatively described. Scaling analysis identifies distinct clogging regimes associated with changes in avalanche size. The variation in stress with avalanche size arises from changes in the effective particle weight, force-chain orientation, and stress transmission coefficient. These results improve the understanding of stress redistribution in clogged silos and may inform future predictions of clogged stress states under different opening conditions.

Results

The link between avalanche size and stress distribution

Particles are initially generated all at once inside a $120d$ long, $30d$ wide, and $1.1d$ thick closed container, where d is the particle diameter (Fig. 1a). Unless otherwise specified, all distances in this study are normalized by the particle diameter d. Non-overlapping (non-contacting), motionless particles are initiated above a bottom opening of size $D = b/d$, where b is the physical orifice width. Different realizations differ only in the particles' initial positions. The particles settle under gravity where some immediately exit through the bottom opening until a clog is formed. During flow, particles near the sidewalls slow down and become increasingly disordered. This structure gradually stabilizes, leading to the development of dead zones near the sidewalls and a clogging arch that halts the flow completely (Fig. S1 in Supplementary Note 1). Clogging is defined as a blockage at the opening which prevents further discharge for more than 2 seconds[31,32]. After the particles settle into a static packing, the free surface height reaches ~$60d$. The number of particles that are released prior to clogging is called the avalanche size s following the terminology used in related literature[27,33,34].

The simulation domain is discretized into unit measurement cells with volume $V_{\mathrm{bin}} = d^3$. Measurements for stresses are obtained from $A = 1 \times 1$ (white) and $A = 6 \times 6$ (blue) cells in Fig. 1a. The stress tensor is nondimensionalized by the weight and size of a single particle, $\boldsymbol{\sigma}' = \frac{\sum_{i=1}^{N} \boldsymbol{F}_i \otimes \boldsymbol{l}_i}{mg/d^2 A V_{\mathrm{bin}}}$, where N is the number of contacts in a cell, $\boldsymbol{F}_i$ is contact force between two particles, $\boldsymbol{l}_i$ is the distance between their center, m is the particle mass. It is then averaged over T number of simulations (i.e. blockage instances) $\boldsymbol{\sigma} = \frac{1}{T}\sum_{j=1}^{T} \boldsymbol{\sigma}_{\boldsymbol{j}}'$[24]. Vertical stress σ_{zz} and σ_{zz}' are the normal components of $\boldsymbol{\sigma}$ and $\boldsymbol{\sigma}'$ along the vertical direction, respectively.

The vertical normal stress σ_{zz} increases along the depth Z due to the accumulation of particle weight (Fig. S2 in Supplementary Note 2). In a closed container ($D = 0.0$), both the vertical and transverse normal stresses σ_{yy} are uniform along the width Y. Fig. 1b shows the σ_{zz} profile at a distance $3d$ away from the right wall Y_1 and along the center of the pile Y_0 for different D. At both locations and for other opening sizes ($D > 0$), σ_{zz} increases towards the bottom of the container in a similar fashion until a depth $Z_{\mathrm{c}} \approx 20$. Beyond Z_{c} (towards the bottom), σ_{zz} becomes sensitive to D in such a way that when the opening is very large, σ_{zz} decreases. This tendency is more evident at Y_0 in which stresses are minimum near the opening. We compare the σ_{zz} profiles with common stress distributions for static granular piles: the liquid stress distribution $\sigma_{zz} = \frac{\rho_{\mathrm{b}} g d}{mg/d^2} Z$ defines a monotonic increase along the depth while the Janssen stress distribution $\sigma_{zz} = \frac{\rho_b g w}{2\mu\zeta mg/d^2}\left(1 - e^{-\frac{2\mu\zeta d}{w}Z}\right)$ captures the stress increase and subsequent saturation due to the sidewall friction where $\rho_{\mathrm{b}} = \phi\rho = 1440$ kg/m^3 is the bulk density of particles, $\mu = 0.3$ is the friction coefficient between particles and between particles and the wall, $\phi = 0.56$ is the solid fraction, $w = 0.3$ m is width of the silo, and $\zeta = 0.9$ is the constant stress coefficient. Both stress distributions assume that σ_{zz} is constant along the Y axis. At $Z \lesssim 20$, σ_{zz} follows both the liquid and Janssen distributions for all D showing that near the free-surface, stresses are only due to the particles' weight. Below Z_{c}, static stress distributions, both at the boundary and at the center, no longer follow the conventional liquid nor Janssen stress distributions.

Fig. 1c shows that the avalanche size s is generally greater and spans over a wider range when D is increased, showing that more particles are released prior to clogging in larger openings. Fig. 1d further shows that the average avalanche size for each silo opening $\langle s \rangle$ in the simulations increases exponentially with D and falls within the range of values obtained in experiments[25,26]. The relationship of $\langle s \rangle$ with D is robust for larger 2-dimensional silos ($154d$ long and $54d$ wide), for 3-dimensional cylindrical silos of various sizes (construction and measurement details in Fig. S6 of the Supplementary Note 4), and for different initiation protocols (particles settle at an initial velocity of 3 m/s), although the $\langle s \rangle$ in the 3-dimensional case is slightly more sensitive to D due to the greater number of particles needed to clog. The shared dependence of s and σ_{zz} on D suggests that the stress distributions are related to the avalanche size. The probability distribution of σ_{zz}'/σ_{zz} does not vary with s and D, which means that the normalized local stress statistics remain invariant, demonstrating that s and D control σ_{zz}' through σ_{zz} (see Fig. S3 in Supplementary Note 3).

To investigate the relationship between s and σ_{zz}, we evaluate the change of σ_{zz} with s for different D measured at larger averaging zones (blue regions) in Fig. 2a-d. σ_{zz} shows a complex dependence on s, D, and with the location at which it is measured, i.e. $\sigma_{zz} = \sigma_{zz}(s, D, Y, Z)$. At low s, σ_{zz} is approximately constant but begins to decline after s exceeding a certain value. σ_{zz} once again evens out to a lower value at a larger threshold. The upper and lower σ_{zz}

limits do not vary with D, but with the location of the averaging area. The difference between the upper and lower σ_{zz} limits at Y_0 and Y_1 decrease moving towards the top. The dependence of σ_{zz} on s, D, and location within the packing remains consistent in the larger two-dimensional silo, under the different initial velocity protocols, and in the three-dimensional classical cylindrical silo (Figs. S4a, S5a, S7a, and S8a in Supplementary Note 4). This shows that the transitional dependence of the vertical normal stress with the avalanche size is robust for different scales and initiation conditions.

Avalanche size dependent clogging regimes and associated micro-parameters

The σ_{zz} decreases non-linearly with increasing s. At low s, σ_{zz} is maximum ($\sigma_{zz}^{\max}$) and declines only when a minimum s is exceeded. Beyond this point, σ_{zz} gradually decreases and approaches a minimum value $\sigma_{zz}^{\min}$ as $s \to \infty$. The decline and saturation of σ_{zz} with s can be captured by the reverse logistic function: $\frac{d\sigma_{zz}}{ds} = k(\sigma_{zz} - \sigma_{zz}^{\max})(\sigma_{zz} - \sigma_{zz}^{\min})$, where k is a constant for a specific D in different average zone. Integration yields:

$$\sigma_{zz} = \sigma_{zz}^{\min} + \frac{\Delta\sigma_{zz}}{1 + \exp(s^*)} \tag{1}$$

where $s^* = k\Delta\sigma_{zz}s - C$, and $\Delta\sigma_{zz} = \sigma_{zz}^{\max} - \sigma_{zz}^{\min}$. The $\sigma_{zz}^{\max}$ is equivalent to the stress in a completely closed container. The term $k\Delta\sigma_{zz}$ controls the sensitivity of σ_{zz} with s. The coefficient C quantifies the impact of the location where σ_{zz} is measured and determines the threshold beyond which σ_{zz} begins to decrease significantly. These two coefficients independently express the effects of slit size and position on σ_{zz} and are obtained through data fitting (solid lines in Fig. 2a-d; other stress-related parameters are shown in Table. 1). The coefficient $k\Delta\sigma_{zz}$ depends only on D and Fig. 3a shows that $\frac{1}{k\Delta\sigma_{zz}}$ varies linearly with D^2. This relationship is insensitive to the silo size, the initial velocity protocol, and dimensionality. Fig. 3(b) shows that the coefficient C increases with the distance $P = \sqrt{(Y - Y_0)^2 + (Z - Z_0)^2}$ from the center of averaging zone to the slit center (Y_0, Z_0). This reflects the tendency of the force-chain structure near the slit to be more easily disturbed by the outflow, whereas particles farther from the slit experience weaker disturbance. The relationship between C and P depends on the dimensionality (see Supplementary Note 4) which indicates that, in the three-dimensions case, greater discharge is required to observe a pronounced change in the stress distribution. These relationships can be summarized as:

$$\frac{1}{k\Delta\sigma_{zz}} = \alpha D^2 + \beta; C = \gamma \ln(P + 1) + \epsilon, \tag{2}$$

where $\alpha = 0.27$, $\beta = 0.40$ for both two and three dimensions, $\gamma = 1.41$, and $\epsilon = 6.15$ for two dimensions while $\gamma = 1.75$, and $\epsilon = 15.32$ for three dimensions.

To account for the influence of the averaging location on the stress measurements, σ_{zz} is further normalized as $\sigma_{zz}^* = \frac{\sigma_{zz} - \sigma_{zz}^{\min}}{\Delta\sigma_{zz}}$ through which Eq. (1) can be re-written as:

$$\sigma_{zz}^* = \frac{1}{1 + \exp(s^*)} \tag{3}$$

Plotting s^* versus σ_{zz}^* collapses all data points covering different D into a single curve as shown in Fig. 4. The normalized curve is asymptotic at 0 and 1 and can be broken down into three regimes representing distinct dependencies on s^*. Regime boundaries are drawn at $s^* = -3$ and $s^* = 3$ corresponding to $\sigma_{zz}^* = 0.95$ and $\sigma_{zz}^* = 0.05$, respectively. (1) When $s^* \lesssim -3$, the number of released particles is so small that the stress distribution still resembles that of a sealed container. (2) When $-3 < s^* \lesssim 3$, the number of discharged particles significantly impacts the stress distributions. (3) When $s^* > 3$, the stresses are at a minimum and σ_{zz} lower than $\sigma_{zz}^{\min}$ may correspond to continuous particle flow without clogging, as the force chain structures in flowing states are weakly connected[22,23]. These regimes in the $s^* - \sigma_{zz}^*$ phase space are termed the *Weak-discharge* (*WD*), the *Moderate-discharge* (*MD*), and *Large discharge* (*LD*) regimes. This scaling also holds for larger-silos, for different preparation protocols and for the large and small three-dimensional cylindrical silos (see Figs. S4b, S5b, S7b and S8b in the Supplementary Note 4).

The results thus far shows that the local stress in a clogged silo of monodisperse dry particles depend on particle properties (ρ, d, μ), gravitational acceleration g, volume fraction ϕ, opening size b through the avalanche size s, measurement-zone position (y, z), container size and geometry, and preparation protocol. In this study, the volume fraction does not significantly change between tests, the friction coefficient μ is fixed, and the local stress is nondimensionalized by the particle weight (combination of ρ, g, d). Lengths are normalized by d, giving $D = b/d$, $Y = y/d$, and $Z = z/d$. The effect of measurement-zone position is further incorporated through P, so the proposed scaling mainly involves D, s, and P. The remaining conditions including container geometry and dimensionality, filling width or radius, filling height, and preparation protocol were examined over relatively broad ranges, as summarized in Supplementary Table S2 of Supplementary Note 5. Additional tests have shown that variations in filling size and preparation protocol have no obvious influence on the normalized scaling s^*, whereas dimensionality affects the fitted relation for C. The scaling relationship is expected to apply when clogged states span a sufficiently wide range of avalanche sizes, so that both $\sigma_{zz}^{\max}$ and $\sigma_{zz}^{\min}$ can be identified. For excessively large openings, such as $D > 5$, clogging may does not occur and $\sigma_{zz}^{\min}$ is therefore undefined, making the logistic scaling inapplicable. When $\Delta\sigma_{zz} \approx 0$, such as at locations above Z_c in Fig. 1b where the local stress is nearly independent of s^*, the logistic transition becomes indistinct.

Classical models for static stress distributions in silos systematically deviate from the stresses when an outlet is present (Fig. 5a, b). Near the walls (Y_1), the stresses corresponding to low s exceed the liquid stress distribution. As s increases, the stresses weaken, approaching the Janssen distribution. Stress distributions at the center (Y_0) exhibit similar transitions across the different regimes except for the observable decrease near the bottom opening. The Janssen model assumes upward wall friction ($-Z$ direction), with fully mobilized lateral wall support and uniform transmission of the stress coefficient throughout the packing. However, our results demonstrate that, for cases with $s > 0$, both the side wall friction $f_{\mathrm{r,s}}$ (Fig. 5c) and the stress coefficient ζ (Fig. S9a in Supplementary Note 6) become spatially heterogeneous. This indicates that the Janssen model is insufficient to capture the intergranular behavior in such cases, thereby violating two core assumptions of Janssen model. Consequently, the Janssen framework fails to capture the evolving stress heterogeneity associated with variations in avalanche size. In contrast, the oriented-stress-linearity (OSL) model relaxes the assumption of uniform stress transmission by aligning stresses with force-chain directions[36–38]. The stress field is expressed in a rotated coordinate system $(\boldsymbol{q}, \boldsymbol{n})$, where $\boldsymbol{q} \perp \boldsymbol{n}$, with the $\boldsymbol{q}$-axis oriented along the force-chain direction. Here, τ denotes the angle between the force chain connecting two particles and the Y_0. In the stress continuity equations:

$$\frac{\partial\sigma_{yy}}{\partial y}+\frac{\partial\sigma_{yz}}{\partial z}=0 \quad (4)$$

$$\frac{\partial\sigma_{yz}}{\partial y}+\frac{\partial\sigma_{zz}}{\partial z}-G=0. \quad (5)$$

are closed by the constitutive relation $\sigma_{yy}=\eta_1\sigma_{zz}+\eta_2\sigma_{yz}\mathrm{sgn}(Y)$, where $\eta_1=\frac{\psi-(\tan\tau)^2}{1-\psi(\tan\tau)^2}$, $\eta_2=\frac{2(\psi+1)\tan\tau}{1-\psi\,(\tan\tau)^2}$, and $\psi=\frac{\sigma_{nn}}{\sigma_{qq}}$ is the stress coefficient in this rotated system. Here, $\mathrm{sgn}(Y)$ is -1 for $Y<Y_0$ and 1 otherwise. The sidewalls exert a frictional force $f_{\mathrm{r,s}}$ (as shown in Fig. 5c), while the front and back walls exert $f_{\mathrm{r,w}}$ (insert in Fig. 5d) both nondimensionalized by $V_{\mathrm{bin}}mg/d^3$. Near the side walls, the boundary condition satisfies: $\sigma_{yz}+f_{\mathrm{r,s}}\mathrm{sgn}(Y)=0$. Away from the sidewalls, the particle weight is supported by $f_{\mathrm{r,w}}$ giving $Gd=\frac{\phi\rho g}{mg/d^3}+f_{\mathrm{r,w}}$, where $Gd>1$ means that grains experience forces exceeding their own weight due to the applied downward shear (overweighted condition) and <1 if the upward shear force supports the granular weight instead (underweighted condition).

Good agreement between the predictions of Eqs. (4–5) and the DEM data (Fig. 5a, b) indicates that the OSL framework accurately captures the measured stress profiles. This agreement demonstrates that the stress state is governed by the microstructural parameters ϕ, $f_{\mathrm{r,s}}$, G, $\tan\tau$ and ψ which are directly obtained from the DEM data (Fig. 5c-f). Although the volume fraction ϕ has been considered in some studies as an important physical quantity affecting force magnitude[2,39], our results show that ϕ increases slightly with increasing s (Fig. S9b and Fig. S10 in Supplementary Note 6), remaining within the narrow range of 0.54–0.57. Its influence on the calculation of G is therefore limited. This shows that regardless of whether the silo clogs instantaneously or after a prolonged flow episode, the local bulk density and particle weight almost remain unchanged.

Fig. 5(c, d) shows that at $Z<20$, the side wall shear $f_{\mathrm{r,s}}\approx 0$ and $Gd\approx 1$ despite increasing s. This indicates that the wall-induced shear force neither compresses nor supports the grains in this region, and thus the granular weight is essentially unaffected by the walls. Meanwhile, $\tan\tau$ and ψ, as shown in Fig. 5(e, f), remain nearly constant at both transverse positions Y_1 and Y_0, suggesting that the force chain orientation remains nearly constant, while the ratio between the stress components parallel and normal to the force chain direction also remains unchanged. These observations indicate that discharge does not affect the frictional interaction between grains and the walls in regions far from the outlet, and that the stress transmission paths remain stable. This behavior is consistent with stress transmission models without wall effects. Consequently, the vertical stress σ_{zz} at both transverse positions Y_1 and Y_0 follows the liquid-like stress distribution (see the insets of Fig. 5a, b).

The region $Z>20$ is primarily governed by discharge-induced disturbances and controlled by s^*. To better show how s^* controls the stress state across the various regimes (Fig. 4), we plot it directly against the relevant OSL micro-parameters in Fig. 6. Fig. 6a, b show that both $f_{\mathrm{r,s}}$ (measured at the sidewalls) and Gd (evaluated in the bulk, away from the walls) exhibit a consistent, regime-dependent response to s^*, reflecting the influence of wall friction despite acting at different locations. In the low s^* (*WD* regime), $f_{\mathrm{r,s}}>0$, meaning the walls impose a compressive shear on the particles, analogous to a reverse Janssen effect[21]. Correspondingly, $Gd>1$, so the bulk is effectively overweighted and σ_{zz} exceeds the liquid stress prediction at both Y_0 and Y_1. As s^* increases into the *MD* regime, the shear direction is reversed ($f_{\mathrm{r,s}} < 0$), possibly due to increased particle–wall slip[21], such that the walls begin to support the particle weight. This transition is reflected in the bulk by $Gd < 1$, indicating an underweighted state. However, the shear is not fully mobilized throughout the packing, and thus departs from the Janssen assumption. In the *LD* regime, both $f_{\mathrm{r,s}}$ and Gd plateau, indicating that wall shear has reached its maximum mobilization and the stress state has saturated across both boundary and bulk regions. Fig. 6c shows that the angle of orientation $\tan\tau$ is not sensitive to s^* near the center $Y_0(Y = 15)$, where the symmetry of the system suppresses any net lateral bias in force-chain orientation. Increasing s^* into the *MD* regime, $\tan\tau$ at $Y_1(Y = 27)$ rises, indicating that the force chains tilt outward toward the side wall, increasingly redirecting the grain weight to the boundaries. Once s^* enters the *LD* regime, local deflection of force chains reaches a maximum since $\tan\tau$ remains unchanged. Fig. 6d shows that ψ increases at Y_0 with increasing s^*. This is because arch that forms near the opening diverts more grain weight toward the side walls, resulting in σ_{zz} that fall below the Janssen prediction as shown in Fig. 5b. In contrast, at Y_1 the decrease of ψ indicates that a greater proportion of the stress is carried along the rotated force-chain direction, with less transferred to the direction normal to it.

Conclusion

In summary, several discrete bodies can be clogged when passing through a narrow opening such as in vertical silos. The stress distribution of clogged, immobile particles is different from that in completely closed vertical containers despite both being in a quasi-static state. Results here show that these stress distributions depend on the size of the opening through the number of particles that escape from it prior to clogging, termed the avalanche size. A scaling analysis based on a defined dimensionless avalanche size s^*, derived from the reverse logistic equation, enables the identification of different clogging regimes. The parameter s^* incorporates information on the opening size ($k\Delta\sigma_{zz}$) and on the position in which the stress is measured (C). When $s^* \leq -3$ (*weak discharge* regime), the stress distribution is unaffected by the avalanche size and is similar to that of a sealed container. As with sealed containers, stresses are controlled by the weight of the pile supported by the shear force provided by the boundary walls. When $-3 < s^* \leq 3$, the stress distribution is influenced by particle discharge (*Moderate-discharge* regime), with stress decreasing near the opening depending on s^*. When $s^* > 3$ (*Large discharge* regime), the stresses are minimum and are independent of s^*.The OSL model further reveals the mechanism underlying the stress reduction with increasing avalanche size under different opening sizes and avalanche sizes. As the avalanche size increases, the supporting shear force exerted by the sidewalls becomes stronger, thereby reducing the effective weight of particles. Meanwhile, force chains near the boundaries gradually deflect toward the sidewalls, allowing more load to be transferred laterally. Near the orifice, the formation of clogging arches further promotes this lateral transfer, leading to a decrease in stress with depth even in the vicinity of the opening.

This study improves the understanding of stress distribution in clogged silos. These results offer insights into static stress distribution in clogged states for different opening size structures, which is important for the design of industrial silos[24,40,41]. Additionally, it enhances the understanding of static stress distribution in granular materials and its dependence on flow history[19]. The composition of real granular flows is inherently complex, often made up of particles that have dissimilar sizes and shapes. More angular particles generally increase the clogging probability because interlocking can readily occur through face-to-face contacts, making clogging more likely than with spherical particles[33,42]. The presence of larger particles in bidisperse or polydisperse mixtures[43,44] is likewise expected to enhance the clogging probability and may increase C. This means that a larger avalanche size would be required to release the stress carried by the particle assembly, and the localized stress heterogeneities would deviate from the predicted distributions. It should also be emphasized that the reverse logistic function adopted in this study is mainly a compact empirical description of the transition between stress and avalanche size observed in the numerical results, rather than the unique theoretical functional form. The key finding of this work is that a stable S-shaped correspondence exists between avalanche size and clogged stress. Although other smooth S-shaped functions, such as the error function, may also provide satisfactory fits, the logistic form retained here is comparatively simple and, more importantly, enables the construction of the normalized avalanche size s^*, which facilitates a unified identification of different clogging regimes.

In our equivalent two-dimensional system, the opening size is restricted to $D \leq 4.5$, within which stable clogging arches can still form. When $D > 5$, clogging rarely occurs, and when it does, it is highly transient. At present, the formation of stable clogging arches in larger orifices is still debated. An interesting question that could be explored in future work is whether a critical opening size exists beyond which no clogging forms[25,26,45,46]. Stress studies under both clogging and non-clogging conditions could also help to reveal the existence of a minimum local stress $\sigma_{zz}^{\min}$. In addition, the physical origin of avalanche size variation deserves further discussion. For example, when the driving force acting on the particles increases, the volume fraction within the granular assembly may increase, which in turn raises the interparticle stress and leads to a larger avalanche size[47]. A clearer understanding of how interparticle stress and volume fraction govern the average avalanche size therefore remains an important topic for future research. The role of friction coefficients is also important, because friction is a key factor controlling the formation of clogging arches, thereby affecting the clogging probability and the avalanche size[4,28]. Moreover, only two preparation protocols were considered in the present study. Other preparation procedures, such as allowing the particles to come to rest before release, or triggering a second clogging event by reopening the outlet after clogging has occurred, may lead to larger avalanche sizes[11,25]. The influence of different preparation protocols on the relationship between avalanche size and stress therefore deserves further investigation. In addition, only a horizontal outlet was considered here. In industrial applications, increasing the outlet angle is a common strategy for reducing clogging, as it produces a sharper outlet geometry and can increase the avalanche size[12]. Accurately predicting the average avalanche size under different outlet angles is therefore of practical importance. Finally, experimental validation remains essential for establishing the generality of the present results. Future work combining photoelastic experiments with systematic analyses of clogged stress distributions and force-chain structures[48,49], together with experimental measurements of avalanche size obtained either by camera-based particle counting with image recognition in two-dimensional systems or by measuring the discharged particle mass[25,26], would help evaluate the applicability of the proposed s^* and may reveal additional controlling factors, thereby further extending the scope of the present conclusions.

Methods

Simulation details

To investigate the role of the avalanche size on the static stress distributions of clogged particles, we conduct discrete element simulations of two-dimensional vertical silos (Fig. 1a). The DEM is implemented using the open-source library LIGGGHTS[50]. Particle interactions are modelled using the Hertz contact model. Modelled particles mimic elastic properties of glass beads[51–55]. Each test comprises 1900 particles that have a density of $\rho = 2570$ kg/m³, size of $d = 0.01$ m, coefficient of restitution of 0.8, sliding friction of $\mu = 0.3$, Young's modulus of 3 Gpa, and Poisson's ratio of 0.25. The simulation timestep is 10^{-6} s and gravity is $g = 10$ m/s^2 pointing along the Z axis.

The particles in the modelled system are confined between two parallel plates which have similar material and contact properties as the particles[3,12,32]. The particles are bounded by parallel plates at the front and back with a distance of $1.1d$. The distance ensures that all particles are arranged in a single layer with negligible overlap[56,57]. The container has a width of $30d$ and a height of $120d$ (Z direction). To maintain a constant granular pile height of ~$60d$, the boundary is set as a periodic boundary in the Z-direction to ensure that particles exiting the bottom opening re-enter from the top. This approach results in a flat packing surface (Fig. 1b), identically to the methods that generate particles directly at the top. The pile height is twice the bottom width to prevent the effect of filling on clogging near the opening, thereby maintaining consistent distribution of avalanche size across different silo dimensions[35,46,58]. The ratio of the opening size to the particle diameter, labelled D, is varied between 0.0, 2.5, 3.0, 3.5, 4.0, 4.5. $D = 0.0$ is a control case where there is no opening and no particles are able to exit. Granular flows within this range of D values are commonly observed to exhibit clogging and are studied as representative cases in the literature[3,12,17,25,26,28,35]. When D exceeds this range, the system typically transitions to a regime characterized by intermittent or entirely uninterrupted flow, with clogging becoming rare or absent[57,59,60]. In order to obtain good statistics, we performed simulations with 6000 simulations for each $D \neq 0.0$ case and 1000 for $D = 0.0$. One simulation refers to an independent process in which the silo is randomly refilled, then discharged, and terminated once a stable clog forms[26,42,61,62].

Data availability

The data supporting the plots and findings of this study are available from the corresponding author upon request.

Code availability

The DEM simulations were conducted using the open source software LIGGGHTS. The relevant model settings, simulation parameters, and procedures are described in the Methods section.

References

1. Corwin, E. I., Jaeger, H. M. & Nagel, S. R. Structural signature of jamming in granular media. *Nature* **435**, 1075–1078 (2005).
2. Liu, A. J. & Nagel, S. R. The Jamming Transition and the Marginally Jammed Solid. *Annu. Rev. Condens. Matter Phys.* **1**, 347–369 (2010).

3. Garcimartín, A., Zuriguel, I., Pugnaloni, L. A. & Janda, A. Shape of jamming arches in two-dimensional deposits of granular materials. *Phys. Rev. E* **82**, 031306 (2010).
4. Lozano, C., Lumay, G., Zuriguel, I., Hidalgo, R. C. & Garcimartín, A. Breaking Arches with Vibrations: The Role of Defects. *Phys. Rev. Lett.* **109**, 068001 (2012).
5. Hidalgo, R. C., Lozano, C., Zuriguel, I. & Garcimartín, A. Force analysis of clogging arches in a silo. *Granular Matter* **15**, 841–848 (2013).
6. Péter, H., Libál, A., Reichhardt, C. & Reichhardt, C. J. O. Crossover from Jamming to Clogging Behaviours in Heterogeneous Environments. *Sci Rep* **8**, 10252 (2018).
7. Helbing, D., Buzna, L., Johansson, A. & Werner, T. Self-organized pedestrian crowd dynamics: experiments, simulations, and design solutions. *Transp. Sci.* **39**, 1–24 (2005).
8. Alonso-Marroquín, F., Busch, J., Chiew, C., Lozano, C. & Ramírez-Gómez, Á. Simulation of counterflow pedestrian dynamics using spheropolygons. *Phys. Rev. E* **90**, (2014).
9. Mankoc, C., Garcimartín, A., Zuriguel, I., Maza, D. & Pugnaloni, L. A. Role of vibrations in the jamming and unjamming of grains discharging from a silo. *Phys. Rev. E* **80**, 11309 (2009).
10. Ashour, A., Wegner, S., Trittel, T., Börzsönyi, T. & Stannarius, R. Outflow and clogging of shape-anisotropic grains in hoppers with small apertures. *Soft Matter* **13**, 402–414 (2017).
11. Gella, D., Zuriguel, I. & Maza, D. Decoupling geometrical and kinematic contributions to the silo clogging process. *Phys. Rev. Lett.* **121**, 138001 (2018).
12. López-Rodríguez, D. *et al.* Effect of hopper angle on granular clogging. *Phys. Rev. E* **99**, 032901 (2019).
13. Wiącek, J. *et al.* Converging orifice used to control the discharge rate of spherical particles from a flat floor silo. *Sci. Rep.* **13**, 669 (2023).
14. Zhang, S., Zeng, Z., Yuan, H., Li, Z. & Wang, Y. Precursory arch-like structures explain the clogging probability in a granular hopper flow. *Commun. Phys.* **7**, (2024).
15. Valdes, J. R. & Santamarina, J. C. Clogging: bridge formation and vibration-based destabilization. *Can. Geotech. J.* **45**, 177–184 (2008).

16. Guo, P. & Zhou, S. Arch in granular materials as a free surface problem: ARCH IN GRANULAR MATERIALS. *Int. J. Numer. Anal. Methods Geomech.* **37**, 1048–1065 (2013).
17. Lozano, C., Zuriguel, I. & Garcimartín, A. Stability of clogging arches in a silo submitted to vertical vibrations. *Phys. Rev. E* **91**, 62203 (2015).
18. Mondal, S. & Sharma, M. M. Role of flying buttresses in the jamming of granular matter through multiple rectangular outlets. *Granular Matter* **16**, 125–132 (2014).
19. Krishnaraj, K. P. & Nott, P. R. The stress in static granular media under gravity. *J. Fluid Mech.* **980**, A10 (2024).
20. Karim, M. Y. & Corwin, E. I. Eliminating friction with friction: 2D janssen effect in a friction-driven system. *Phys. Rev. Lett.* **112**, 188001 (2014).
21. Mahajan, S. *et al.* Reverse Janssen Effect in Narrow Granular Columns. *Phys. Rev. Lett.* **124**, 128002 (2020).
22. Staron, L., Lagrée, P.-Y. & Popinet, S. The granular silo as a continuum plastic flow: the hour-glass vs the clepsydra. *Phys. Fluids* **24**, 103301 (2012).
23. Vamsi Krishna Reddy, A., Kumar, S. & Anki Reddy, K. Granular particle-shape heterogeneous mixtures discharging through a silo. *J. Fluid Mech.* **912**, A22 (2021).
24. Blanco-Rodríguez, R. & Pérez-Ángel, G. Stress distribution in two-dimensional silos. *Phys. Rev. E* **97**, 12903 (2018).
25. Janda, A., Zuriguel, I., Garcimartín, A., Pugnaloni, L. A. & Maza, D. Jamming and critical outlet size in the discharge of a two-dimensional silo. *Europhys. Lett.* **84**, 44002 (2008).
26. To, K. Jamming transition in two-dimensional hoppers and silos. *Phys. Rev. E* **71**, 060301 (2005).
27. Zuriguel, I., Pugnaloni, L. A., Garcimartín, A. & Maza, D. Jamming during the discharge of grains from a silo described as a percolating transition. *Phys. Rev. E* **68**, 030301 (2003).
28. To, K., Lai, P.-Y. & Pak, H. K. Jamming of granular flow in a two-dimensional hopper. *Phys. Rev. Lett.* **86**, 71–74 (2001).

29. Tewari, S., Dichter, M. & Chakraborty, B. Signatures of incipient jamming in collisional hopper flows. *Soft Matter* **9**, 5016 (2013).

30. Sielamowicz, I., Czech, A. & Kowalewski, T. A. Comparative analysis of empirical descriptions of eccentric flow in silo model by the linear and nonlinear regressions. *Powder Technol.* **270**, 393–410 (2015).

31. Zhang, S. *et al.* Numerical investigation on the clogging-collapsing events in granular discharge. *Powder Technology* **408**, 117714 (2022).

32. Merrigan, C., Birwa, S. K., Tewari, S. & Chakraborty, B. Ergodicity breaking dynamics of arch collapse. *Phys. Rev. E* **97**, 040901 (2018).

33. Zuriguel, I. *et al.* Clogging transition of many-particle systems flowing through bottlenecks. *Sci Rep* **4**, 7324 (2015).

34. Masuda, T., Nishinari, K. & Schadschneider, A. Critical Bottleneck Size for Jamless Particle Flows in Two Dimensions. *Phys. Rev. Lett.* **112**, 138701 (2014).

35. Arévalo, R. & Zuriguel, I. Clogging of granular materials in silos: effect of gravity and outlet size. *Soft Matter* **12**, 123–130 (2016).

36. Wittmer, J. P., Claudin, P., Cates, M. E. & Bouchaud, J.-P. An explanation for the central stress minimum in sand piles. *Nature* **382**, 336–338 (1996).

37. Wittmer, J. P., Cates, M. E. & Claudin, P. Stress propagation and arching in static sandpiles. *J. Phys. I* **7**, 39–80 (1997).

38. Vanel, L. *et al.* Stresses in silos: comparison between theoretical models and new experiments. *Phys. Rev. Lett.* **84**, 1439–1442 (2000).

39. Ikeda, A., Berthier, L. & Sollich, P. Unified study of glass and jamming rheology in soft particle systems. (2012).

40. Gandia, R. M., Gomes, F. C., Paula, W. C. de, Oliveira Junior, E. A. de & Aguado Rodriguez, P. J. Static and dynamic pressure measurements of maize grain in silos under different conditions. *Biosyst. Eng.* **209**, 180–199 (2021).

41. Thorens, L., Måløy, K. J., Bourgoin, M. & Santucci, S. Magnetic Janssen effect. *Nat Commun* **12**, 2486 (2021).

42. Hafez, A. *et al.* The effect of particle shape on discharge and clogging. *Sci. Rep.* **11**, 3309 (2021).

43. Gray, J. M. N. T. & Chugunov, V. A. Particle-size segregation and diffusive remixing in shallow granular avalanches. *J. Fluid Mech.* **569**, 365 (2006).

44. Cui, K. F. E., Zhou, G. G. D. & Jing, L. Viscous effects on the particle size segregation in geophysical mass flows: insights from immersed granular shear flow simulations. *J. Geophys. Res.: Solid Earth* **126**, (2021).

45. Thomas, C. C. & Durian, D. J. Fraction of clogging configurations sampled by granular hopper flow. *Phys. Rev. Lett.* **114**, 178001 (2015).

46. Arévalo, R. Collisional regime during the discharge of a two-dimensional silo. *Phys. Rev. E* **105**, 044901 (2022).

47. Arévalo, R., Zuriguel, I., Maza, D. & Garcimartín, A. Role of driving force on the clogging of inert particles in a bottleneck. *Phys. Rev. E* **89**, 42205 (2014).

48. Park, K.-H., Baek, S.-H. & Jung, Y.-H. Investigation of arch structure of granular assembly in the trapdoor test using digital RGB photoelastic analysis. *Powder Technol.* **366**, 560–570 (2020).

49. Fang, Y., Guo, L. & Hou, M. Arching effect analysis of granular media based on force chain visualization. *Powder Technol.* **363**, 621–628 (2020).

50. Kloss, C., Goniva, C., Hager, A., Amberger, S. & Pirker, S. Models algorithms and validation for open source DEM and CFD-DEM. *Progress in Computational Fluid Dynamics* **12**, 140–152 (2012).

51. Li, N., Zhou, G. G. D., Hu, H., Cui, K. F. E. & Huang, Y. Influence of trapping efficiency on the pile-up geometry of granular flows behind slit dams. *Engineering Geology* **326**, 107333 (2023).

52. Karabulut, M. *et al.* Mechanical and structural properties of phosphate glasses. *Journal of Non-Crystalline Solids* **288**, 8–17 (2001).

53. Kurkjian, C. R., Gupta, P. K., Brow, R. K. & Lower, N. The intrinsic strength and fatigue of oxide glasses. *Journal of Non-Crystalline Solids* **316**, 114–124 (2003).

54. Watkins, I. G. & Prado, M. Mechanical Properties of Glass Microspheres. *Procedia Materials Science* **8**, 1057–1065 (2015).

55. Vollenberg, P. H. T. & Heikens, D. Particle size dependence of the Young's modulus of filled polymers: 1. Preliminary experiments. *Polymer* **30**, 1656–1662 (1989).

56. Zuriguel, I. *et al.* Silo Clogging Reduction by the Presence of an Obstacle. *Phys. Rev. Lett.* **107**, 278001 (2011).

57. Janda, A., Zuriguel, I. & Maza, D. Flow Rate of Particles through Apertures Obtained from Self-Similar Density and Velocity Profiles. *Phys. Rev. Lett.* **108**, 248001 (2012).

58. Kunte, A., Doshi, P. & Orpe, A. V. Spontaneous jamming and unjamming in a hopper with multiple exit orifices. *Phys. Rev. E* **90**, 20201 (2014).

59. Rubio-Largo, S. M., Janda, A., Maza, D., Zuriguel, I. & Hidalgo, R. C. Disentangling the free-fall arch paradox in silo discharge. *Phys. Rev. Lett.* **114**, 238002 (2015).

60. Kozlowski, R. & Pugnaloni, L. A. Flow rate from a vertical silo with a tilted orifice. *Powder Technol.* **465**, 121189 (2025).

61. Guariguata, A. *et al.* Jamming of particles in a two-dimensional fluid-driven flow. *Phys. Rev. E* **86**, 61311 (2012).

62. Goldberg, E., Manuel Carlevaro, C. & Pugnaloni, L. A. Clogging in two-dimensions: effect of particle shape. *J. Stat. Mech: Theory Exp.* **2018**, 113201 (2018).

Acknowledgements

The authors thank Jens M. Turowski and Anne Mangeney for their valuable suggestions on the manuscript.

Funding

G.G.D.Z. discloses support from the National Key R&D Program of China (2024YFE0104200), the National Natural Science Foundation of China (U24A20618), and the Sichuan Science and Technology Program (2024NSFJQ0043). G.G.D.Z. and J.Z. disclose support from the Strategic Priority Research Program of the Chinese Academy of Sciences (XDB1390200). K.F.E.C. discloses support from the National Natural Science Foundation of China (12572471).

Author contributions

G.G.D.Z. acquired funding, supervised the project, and contributed to the simulation design. N.L. performed the simulations, analyzed the data, and wrote the manuscript. K.F.E.C. analyzed the data and contributed to manuscript writing. J.Z. and L.J. discussed the results and reviewed the manuscript. X.L. and Y.X. provided manuscript suggestions.

Competing interests

The authors declare no competing interests.

Fig. 1 Numerical setup, stress distributions, and avalanche size statistics. (a) Sketch of the numerical simulation setup. The simulation domain is divided into grids for measurement of relevant quantities. Averaged quantities are calculated in the zones shaded in blue (labelled L_0-L_1 and H_0-H_1). (b) Stress distributions near the sidewalls Y_1 ($3d$ away from right side wall) and the center Y_0 of containers with different D. (c) Probability density function (PDF) of avalanche size s. (d) The relationship between averaged avalanche size $\langle s \rangle$ and D, where red and blue dashed line show the relationship proposed by Janda *et al.* (2008) and To (2005), respectively.

Fig. 2 Dependence of local stress on avalanche size. The change of vertical normal stress σ_{zz} with the avalanche size s at locations (a) L_0, (b) H_0, (c) L_1, and (d) H_1 (see Fig. 1). Solid lines are best-fits from Eq. (1).

Fig. 3 Scaling parameters for clogged stress. (a) The relationship between $1/k\Delta\sigma_{zz}$ and the squared of the opening size D^2. (b) The relationship between coefficients C and P. Solid lines are best-fits from Eq. (2).

Fig. 4 The relationship between σ_{zz}^* and s^*. Vertical dashed lines separate three regions: *weak discharge* regime (*WD*), *Moderate-discharge* regime (*MD*), *Large discharge* regime (*LD*). The red solid line is the best fit curve obtained from Eq. (3).

Fig. 5. Spatial variation of physical quantities controlling stress distributions. Stress distributions for $D = 3.5$ at locations (a) Y_1 and (b) Y_0. The solid lines represent the numerical solution of Eqs. (4, 5), while red and blue dashed lines represent the liquid and Janssen stress distributions, respectively. (c) The change of the shear force $f_{\mathrm{r,s}}$ at the right wall with s. Legend at the top indicates the direction of shear force. (d) Change of the effective weight Gd with s for Y_1 and Y_0. Inset in (d) shows shear force $f_{\mathrm{r,w}}$ from front or back walls on particles. (e) Force chain angle (represented through $\tan\tau$) and (f) stress coefficient ψ varied with s for Y_1 and Y_0. The gray dash lines in (c), (d) and (e) indicate $f_{\mathrm{r,s}} = 0$, $Gd = 1$ and $\tan\tau = 0$, respectively.

Fig. 6. Dependence of stress controlling physical quantities on normalized avalanche size. The relationship between the OSL model parameters (a) $f_{\mathrm{r,s}}$, (b) Gd, (c) $\tan\tau$, and (d) ψ with s^*. The dashed lines separate the clogging regimes as shown in Fig. 4. Data averaged over different values of D, whereas the non-averaged data for each individual D are provided separately in Fig. S11 of the Supplementary Note 7.

Table. 1 $\sigma_{zz}^{\max}$ and $\sigma_{zz}^{\min}$ values at different measurement locations.

Measurement cell	$\sigma_{zz}^{\max}$	$\sigma_{zz}^{\min}$
L_0	63.32	19.06
H_0	46.50	28.23
L_1	70.05	44.78
H_1	47.42	33.67

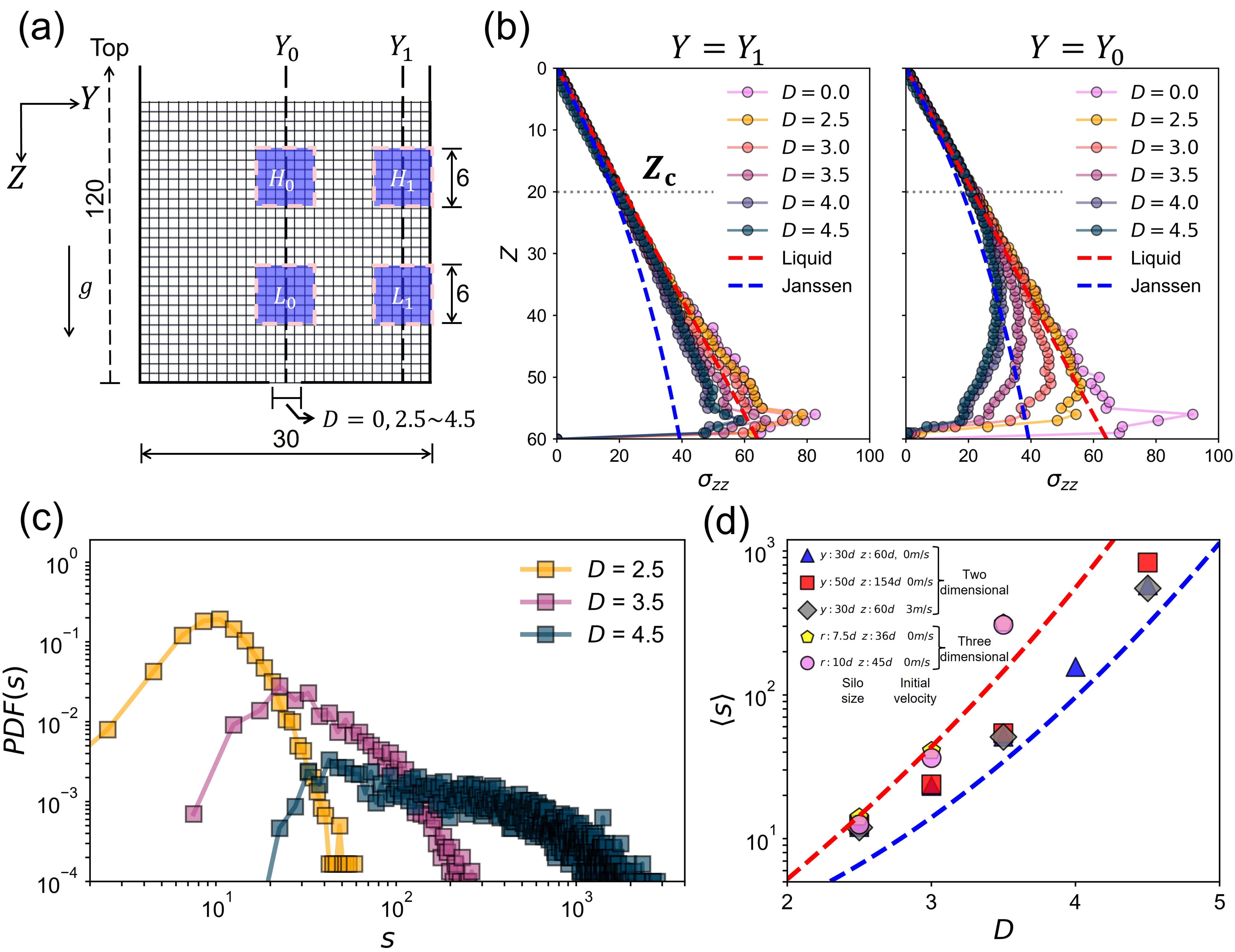

(a)
Top
Y_0
Y_1
Y
Z
120
H_0
H_1
6
g
L_0
L_1
6
$D = 0, 2.5\sim4.5$
30
(b)
$Y = Y_1$
$Y = Y_0$
Z_c
$D = 0.0$
$D = 2.5$
$D = 3.0$
$D = 3.5$
$D = 4.0$
$D = 4.5$
Liquid
Janssen
Z
σ_{zz}
(c)
$D = 2.5$
$D = 3.5$
$D = 4.5$
$PDF(s)$
s
(d)
$y:30d\ z:60d,\ 0m/s$
$y:50d\ z:154d\ 0m/s$
$y:30d\ z:60d\ 3m/s$
Two dimensional
$r:7.5d\ z:36d\ 0m/s$
$r:10d\ z:45d\ 0m/s$
Three dimensional
Silo size
Initial velocity
$\langle s \rangle$
D

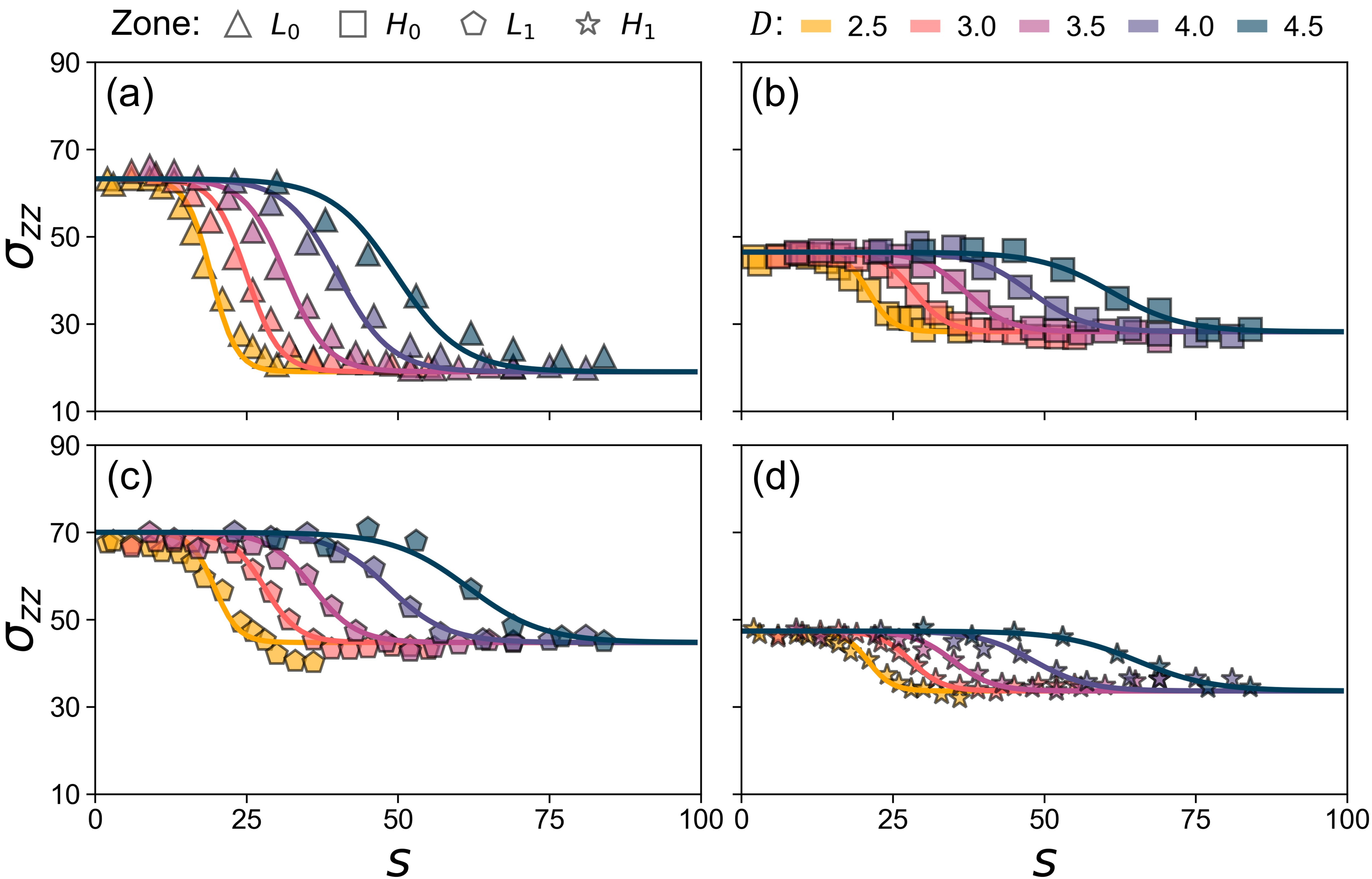
Zone: L_0 H_0 L_1 H_1
D: 2.5 3.0 3.5 4.0 4.5
(a)
(b)
(c)
(d)
σ_{zz}
σ_{zz}
90
70
50
30
10
90
70
50
30
10
0
25
50
75
100
0
25
50
75
100
s
s

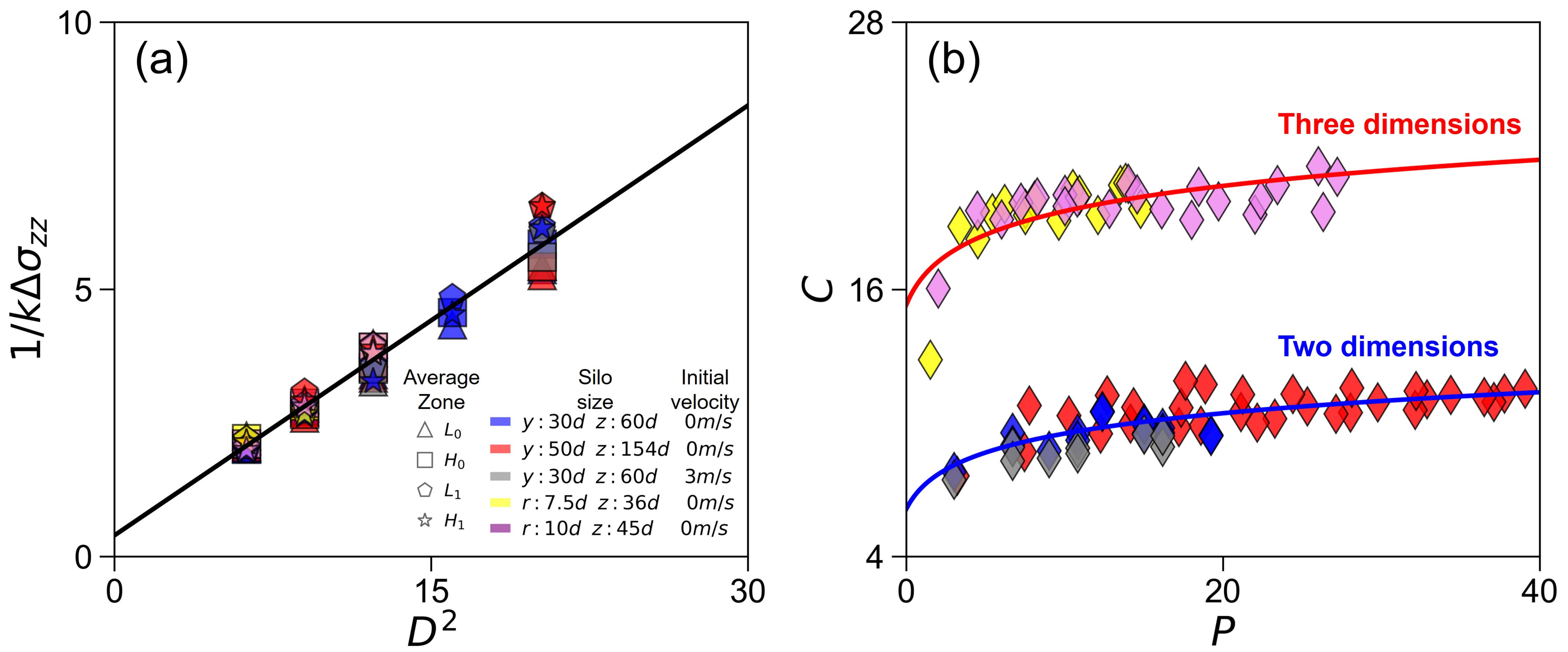

(a)
$1/k\Delta\sigma_{zz}$
D^2
0
5
10
0
15
30
Average Zone
L_0
H_0
L_1
H_1
Silo size
Initial velocity
$y:30d$ $z:60d$ $0m/s$
$y:50d$ $z:154d$ $0m/s$
$y:30d$ $z:60d$ $3m/s$
$r:7.5d$ $z:36d$ $0m/s$
$r:10d$ $z:45d$ $0m/s$
(b)
C
P
4
16
28
0
20
40
Three dimensions
Two dimensions

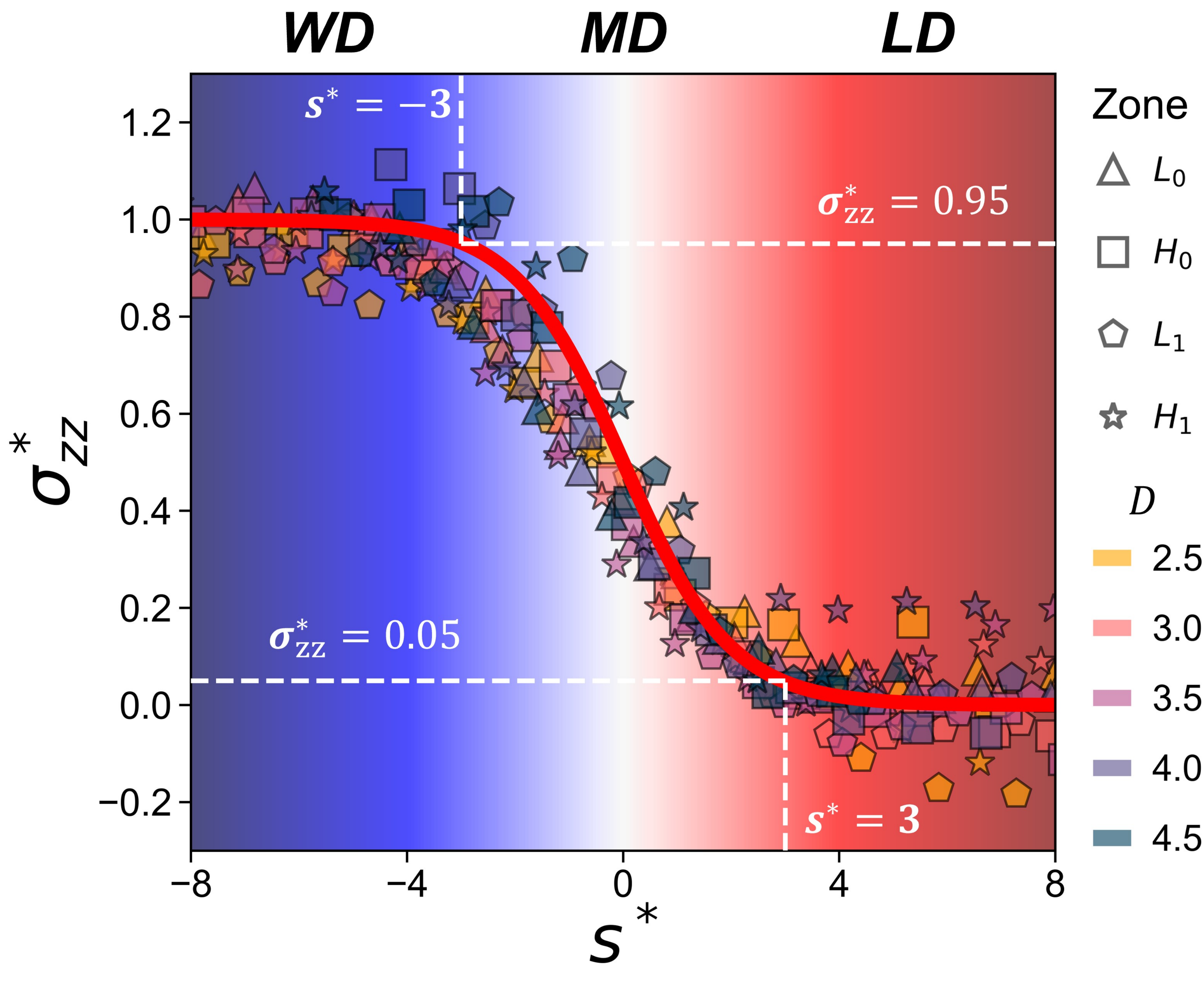
WD
MD
LD
$s^* = -3$
$\sigma^*_{zz} = 0.95$
$\sigma^*_{zz} = 0.05$
$s^* = 3$
1.2
1.0
0.8
0.6
0.4
0.2
0.0
−0.2
−8
−4
0
4
8
σ^*_{zz}
s^*
Zone
L_0
H_0
L_1
H_1
D
2.5
3.0
3.5
4.0
4.5

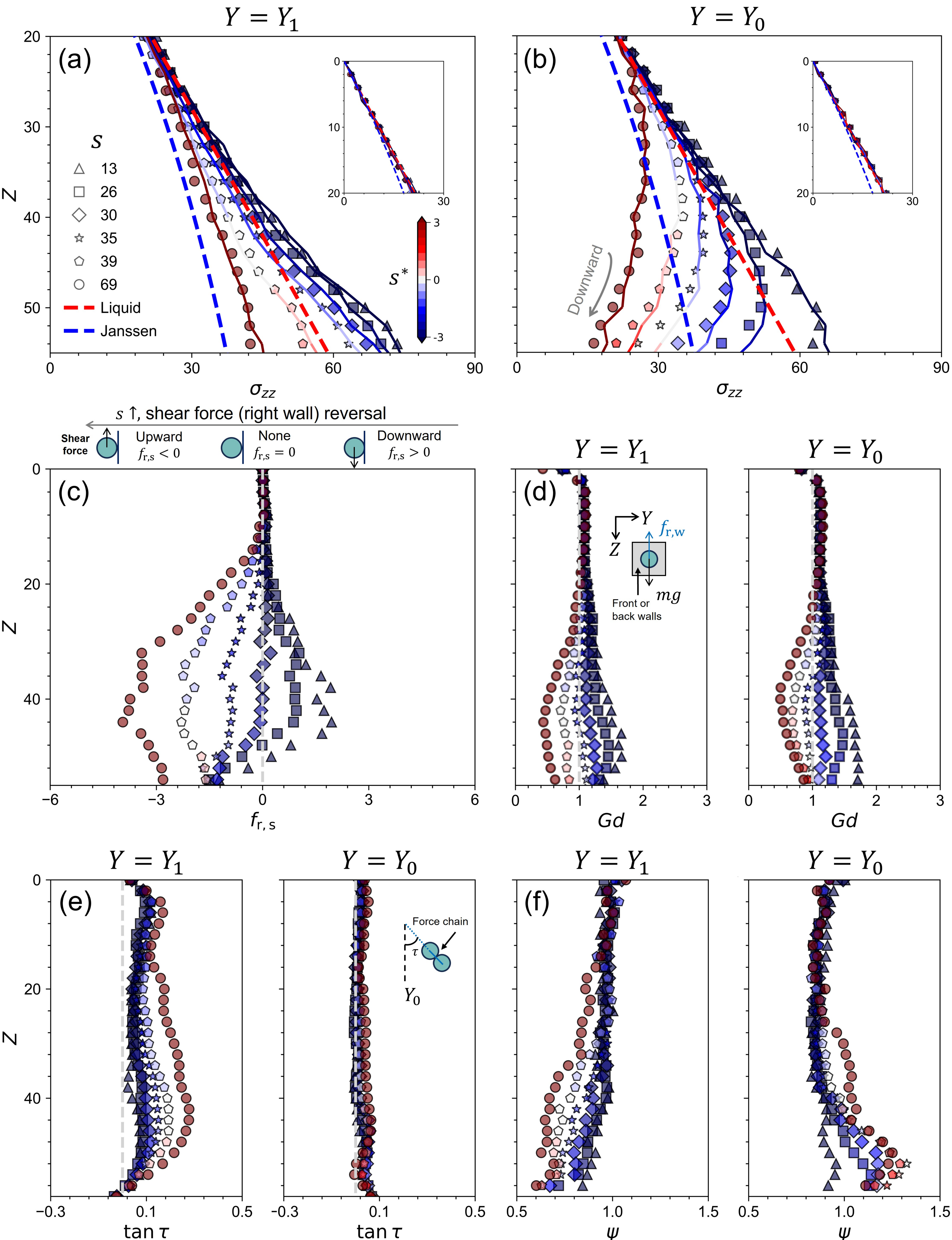

$Y = Y_1$
$Y = Y_0$
(a)
(b)
(c)
(d)
(e)
(f)
s
13
26
30
35
39
69
Liquid
Janssen
s^*
Downward
σ_{zz}
Z
s ↑, shear force (right wall) reversal
Shear force
Upward $f_{r,s} < 0$
None $f_{r,s} = 0$
Downward $f_{r,s} > 0$
$f_{r,s}$
Gd
$f_{r,w}$
mg
Front or back walls
Force chain
τ
Y_0
$\tan \tau$
ψ

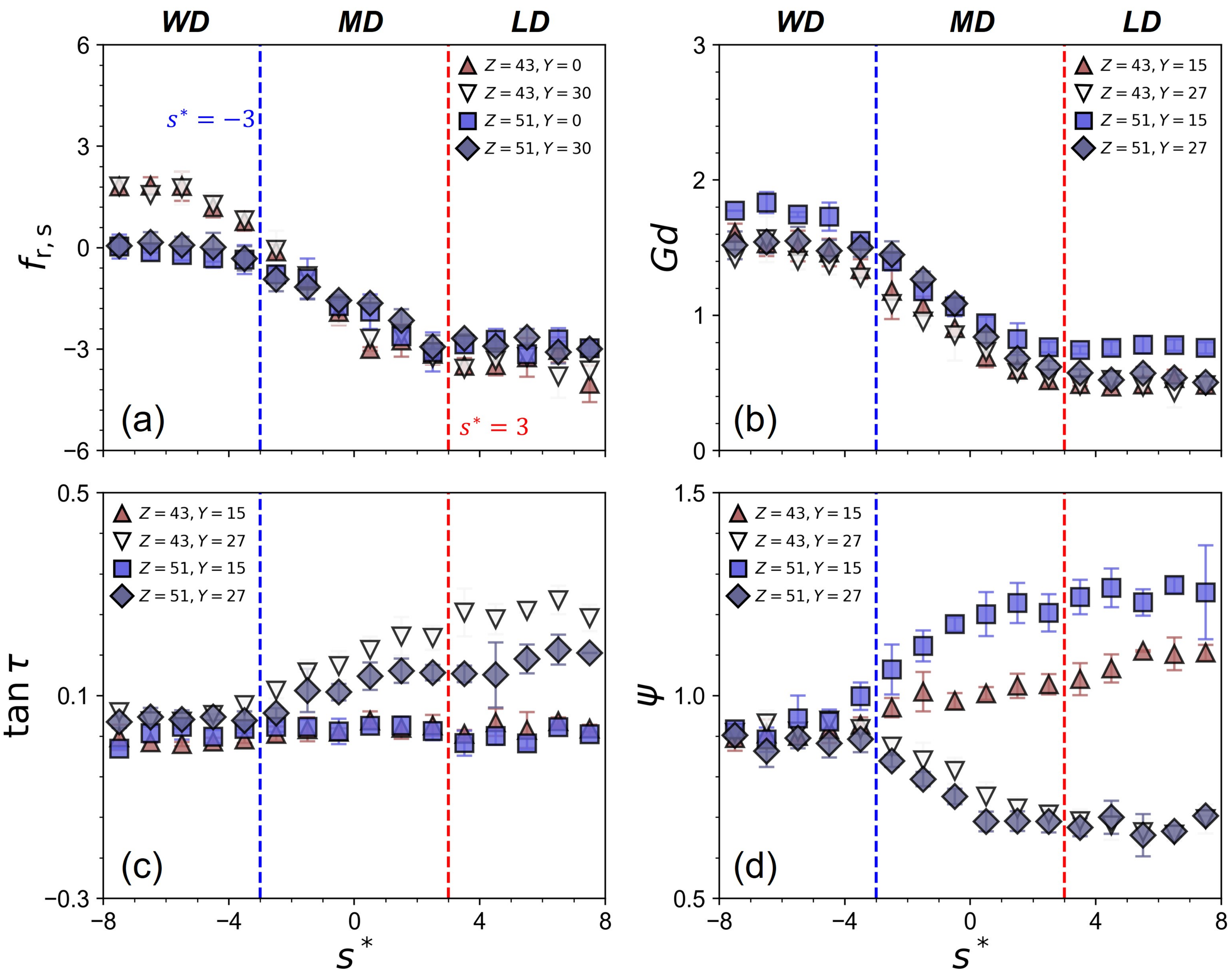
WD
MD
LD
$s^* = -3$
$s^* = 3$
$Z = 43, Y = 0$
$Z = 43, Y = 30$
$Z = 51, Y = 0$
$Z = 51, Y = 30$
$Z = 43, Y = 15$
$Z = 43, Y = 27$
$Z = 51, Y = 15$
$Z = 51, Y = 27$
$f_{r,s}$
Gd
$\tan\tau$
ψ
s^*
(a)
(b)
(c)
(d)